JACS
JOURNAL OF THE AMERICAN CHEMICAL SOCIETY
Article
pubs.acs.org/JACS

Spectroscopic and Computational Investigations of a Mononuclear Manganese(IV)-Oxo Complex Reveal Electronic Structure Contributions to Reactivity

Domenick F. Leto, Allyssa A. Massie, Derek B. Rice, and Timothy A. Jackson*

Department of Chemistry and Center for Environmentally Beneficial Catalysis, University of Kansas, Lawrence, Kansas 66045, United States

Supporting Information

ABSTRACT: The mononuclear Mn(IV)-oxo complex $[Mn^{IV}(O)(N4py)]^{2+}$, where N4py is the pentadentate ligand *N*,*N*-bis(2-pyridylmethyl)-*N*-bis(2-pyridyl)methylamine, has been proposed to attack C−H bonds by an excited-state reactivity pattern [Cho, K.-B.; Shaik, S.; Nam, W. *J. Phys. Chem. Lett.* **2012**, *3*, 2851−2856 (DOI: 10.1021/jz301241z)]. In this model, a ^{4}E excited state is utilized to provide a lower-energy barrier for hydrogen-atom transfer. This proposal is intriguing, as it offers both a rationale for the relatively high hydrogen-atom-transfer reactivity of $[Mn^{IV}(O)(N4py)]^{2+}$ and a guideline for creating more reactive complexes through ligand modification. Here we employ a combination of electronic absorption and variable-temperature magnetic circular dichroism (MCD) spectroscopy to experimentally evaluate this excited-state reactivity model. Using these spectroscopic methods, in conjunction with time-dependent density functional theory (TD-DFT) and complete-active space self-consistent-field calculations (CASSCF), we define the ligand-field and charge-transfer excited states of $[Mn^{IV}(O)(N4py)]^{2+}$. Through a graphical analysis of the signs of the experimental *C*-term MCD signals, we unambiguously assign a low-energy MCD feature of $[Mn^{IV}(O)(N4py)]^{2+}$ as the ^{4}E excited state predicted to be involved in hydrogen-atom-transfer reactivity. The CASSCF calculations predict enhanced Mn^{III}-oxyl character on the excited-state ^{4}E surface, consistent with previous DFT calculations. Potential-energy surfaces, developed using the CASSCF methods, are used to determine how the energies and wave functions of the ground and excited states evolved as a function of Mn═O distance. The unique insights into ground- and excited-state electronic structure offered by these spectroscopic and computational studies are harmonized with a thermodynamic model of hydrogen-atom-transfer reactivity, which predicts a correlation between transition-state barriers and driving force.

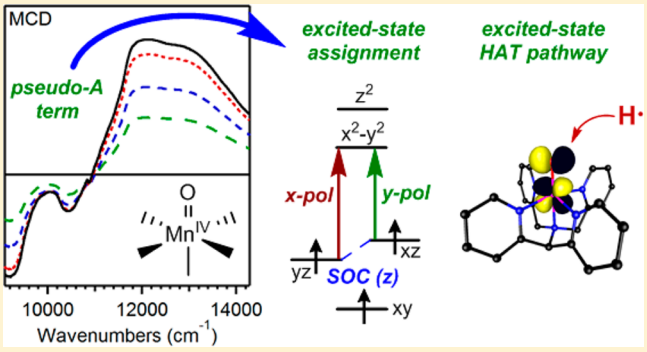

INTRODUCTION

High-valent metal-oxo adducts are common intermediates in hydrogen-atom-transfer and oxygen-atom-transfer reactions in biological and synthetic systems.[1−20] These processes often afford oxygenated products, such as alcohols or epoxides, but reactions initiated by hydrogen-atom transfer can also result in substrate desaturation or halogenation.[21−30] The rates of hydrogen-atom-transfer reactions have been shown to be determined largely by their thermodynamic driving force,[5,31,32] and detailed spectroscopic and computational investigations, predominantly of Fe^{IV}-oxo species, have emphasized modulation of reactivity due to electronic structure perturbations.[12−14,24,33−37] Density functional theory (DFT) studies of hydrogen-atom-transfer processes by nonheme Fe^{IV}-oxo units underscore electronic structure contributions to reactivity, as these computations commonly require the consideration of both S = 1 and S = 2 spin surfaces (so-called two-state reactivity), the relative energies of which are strongly modulated by the ligand field. Although most synthetic, nonheme Fe^{IV}-oxo complexes have S = 1 ground states,[6,9] DFT studies often predict crossing to an S = 2 spin surface to traverse a lower-barrier transition state for hydrogen-atom transfer.[12,37] Thus, a comprehensive understanding of reactivity requires knowledge of the thermodynamics of the hydrogen-atom-transfer process and an understanding of the electronic structure of the metal-oxo species.

Although Mn^{IV}-oxo complexes have traditionally been viewed as less reactive than Fe^{IV}-oxo or Mn^{V}-oxo species, work by Nam[38−40] and our group[41] has shown that Mn^{IV}-oxo species supported by aminopyridyl ligands, such as $[Mn^{IV}(O)(N4py)]^{2+}$ (N4py = *N*,*N*-bis(2-pyridylmethyl)-*N*-bis(2-pyridyl)methylamine; see Scheme 1), can attack relatively strong C−H bonds at reaction rates comparable to those of analogous Fe^{IV}-oxo complexes. Along these lines, Nam has also shown that Mn^{IV}-oxo reactivity can be greatly impacted through the addition of strong Bronsted acids,[42] such as triflic acid, or the Lewis acid Sc^{III}.[40,43] Nonetheless, the basis for the high

Received: August 18, 2016
Published: November 1, 2016

DOI: 10.1021/jacs.6b08661
J. Am. Chem. Soc. 2016, 138, 15413−15424

Scheme 1. Qualitative Reaction Coordinate for Hydrogen-Atom Transfer between $[Mn^{IV}(O)(N4py)]^{2+}$ (Bottom, Left) and a Hydrocarbon, H−R, Based on DFT Computations Described in Ref 51, Showing the Ground State ($^4B_1$) and Lowest-Lying Quartet Excited State (^4E) of the Reactant Complex; Electron Configurations for $^4B_1$ and ^4E Are on the Far Left

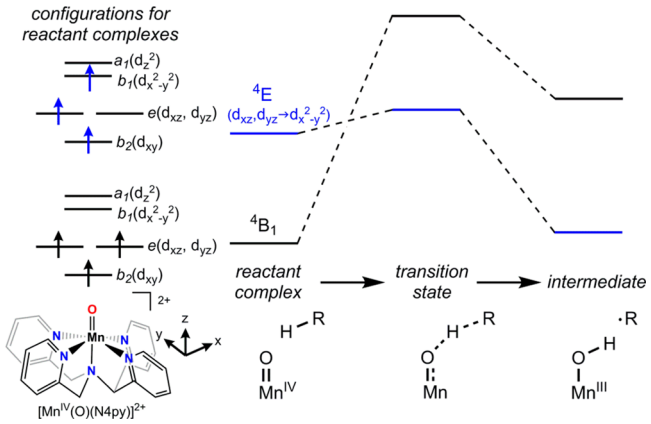

reactivity of these Mn^{IV}-oxo complexes remains unclear. Given the relevance of Mn^{IV}-oxo species to biological and synthetic catalysts,[44−48] this is an important gap in knowledge. We have noted that $[Mn^{IV}(O)(N4py)]^{2+}$ has a $Mn^{IV/III}$ reduction potential ∼700 mV higher than those of several other Mn^{IV}═O complexes.[41] This would be compatible with a larger thermodynamic driving force[31,49,50] and thus a faster hydrogen-atom-transfer rate. However, the driving force for hydrogen-atom transfer depends on the reduction potential *and* the pK_a of the protonated, reduced metal complex.[31,50] As the pK_a of $[Mn^{III}(OH)(N4py)]^{2+}$ has not been measured, the driving force is unknown, and the basis for the high reactivity of this complex remains poorly defined.

Recently, Nam and Shaik have proposed that the hydrogen-atom-transfer landscape of these Mn^{IV}-oxo species involves multiple electronic surfaces,[51] and similar predictions have been made regarding their oxygen-atom-transfer reactivity.[39] The results of DFT computations of the hydrogen-atom-transfer reactions are summarized in Scheme 1. The computations predict hydrogen-atom transfer to proceed initially from the $^4B_1$ ground state, arising from a $b_2(d_{xy})^1e(d_{xz}, d_{yz})^2$ configuration (using the idealized C_{4v} symmetry label). [For these complexes, the $e(d_{xz}, d_{yz})$ orbitals are destabilized relative to $b_2(d_{xy})$, as the former orbitals are strongly Mn═O π-antibonding, whereas $b_2(d_{xy})$ is essentially nonbonding. Along the same lines, the $a_1(d_{z^2})$ orbital is strongly Mn═O σ-antibonding and therefore at higher energy than the Mn−N4py σ-antibonding $b_1(d_{x^2-y^2})$ orbital. See Scheme 1 for a ligand-field splitting diagram.] However, the transition state on the $^4B_1$ surface is quite high in energy, and a lower transition state is offered by a ^4E excited state arising from a $b_2(d_{xy})^1e(d_{xz}, d_{yz})^1b_1(d_{x^2-y^2})^1$ configuration. This configuration is related to the ground state by an $e(d_{xz}, d_{yz}) \rightarrow b_1(d_{x^2-y^2})$ one-electron excitation, and this state was proposed to carry significant Mn^{III}-oxyl character.[51] Thus, according to this model, hydrogen-atom transfer for $[Mn^{IV}(O)(N4py)]^{2+}$ is facilitated by a crossing to this higher-energy surface with oxyl radical character. Although intriguing, and consistent with the available kinetic data, this model has not been subjected to broader scrutiny.

Investigations of Fe^{IV}-oxo reactivity have relied on strong synergy between kinetic studies, computationally derived reaction coordinates, and electronic structure descriptions developed on the basis of spectroscopic data.[6,9,12,33,37] In particular, Solomon and co-workers[11,12,33−36] and Neese and co-workers[52] have shown that combining electronic absorption and magnetic circular dichroism (MCD) experiments with DFT and/or CASSCF computations provides powerful insight into the electronic states governing the reactivity of nonheme Fe^{IV}-oxo centers. While the corresponding hydrogen-atom-transfer reactivity of Mn^{IV}-oxo complexes have been subjected to detailed computational studies[39,51] and kinetic interrogation,[40−42,53] thorough spectroscopic studies of the relevant electronic states are less common. Mn K-edge X-ray absorption[38,41,54−56] and electron paramagnetic resonance (EPR) spectroscopies[57−60] have been used with success to establish metric parameters and ground-state ZFS parameters, respectively, for mononuclear Mn^{IV}-oxo species. The area and energies of X-ray pre-edge features can be related to Mn═O bonding and Mn^{IV} geometry,[54] and EPR experiments using ^{17}O-labeled Mn-oxo species have been used to determine spin delocalization for a high-spin Mn^{V}-oxo species.[58] However, there are comparatively fewer experimental investigations of the low-lying excited states that are relevant to DFT-computed reaction coordinates. We have previously shown the power of combined electronic absorption, MCD, and variable-temperature, variable-field (VTVH) MCD methods in assigning ligand-field excited states for the mononuclear Mn^{IV}-oxo complex $[Mn^{IV}(O)(OH)(Me_2EBC)]^{2+}$, which contains a hydroxo *cis* to the oxo ligand and a neutral N_4 ligand (Me_2EBC = 4,11-dimethyl-1,4,8,11-tetraazabicyclo[6.6.2]-hexadecane).[61] These electronic transitions were then used to compare π- and σ-bonding between this Mn^{IV}-oxo species and its Mn^{IV}-dihydroxo analogue, $[Mn^{IV}(OH)_2(Me_2EBC)]^{2+}$. However, the $[Mn^{IV}(O)(OH)(Me_2EBC)]^{+}$ complex is rather sluggish in C−H bond oxidation,[15,62−64] reacting with dihydroanthracene ∼200-fold slower than $[Mn^{IV}(O)(N4py)]^{2+}$ at comparable temperatures.[62,65] Recent DFT studies of the hydrogen-atom abstraction of the related $[Mn^{IV}(O)_2(Me_2EBC)]$ complex suggest single-state reactivity (i.e., an excited quartet state is *not* involved).[66]

In this work, we investigate the electronic structure of $[Mn^{IV}(O)(N4py)]^{2+}$ through a combination of electronic absorption and MCD experiments, which are complemented by DFT and CASSCF computations. In our analysis, we have spectroscopically identified the low-lying quartet excited state proposed to influence the hydrogen-atom and oxygen-atom-transfer reactivity of this complex. A graphical analysis of MCD *C*-term signs, and the results of TD-DFT and CASSCF calculations, allow us to assign the electronic excited states of $[Mn^{IV}(O)(N4py)]^{2+}$. CASSCF computations, with NEVPT2 corrections, performed as a function of the Mn═O bond length offer insights into how the ground- and excited-state potential-energy surfaces evolve along this reaction coordinate in the absence of substrate, which is relevant for both hydrogen-atom and oxygen-atom-transfer chemistry. Through this approach, we are able to corroborate theoretical predictions of Mn^{IV}-oxo reactivity and relate the electronic structure of different states to the thermodynamic driving force for the hydrogen-atom-transfer process.

DOI: 10.1021/jacs.6b08661
J. Am. Chem. Soc. 2016, 138, 15413−15424

MATERIALS AND METHODS

MCD Sample Preparation and Data Collection. A 7.5 mM MCD sample of $[Mn^{IV}(O)(N4py)]^{2+}$ was prepared from a 15 mM CF_3CH_2OH solution of $[Mn^{IV}(O)(N4py)]^{2+}$ that was diluted to 7.5 mM with ethanol to form a glassy solvent mixture with CF_3CH_2OH:CH_3CH_2OH (50:50). The specific procedure is as follows. A 1.0 mL CF_3CH_2OH suspension containing 2.5 equiv of PhIO (16.5 mg, 0.3 mmol) was added to a 1.0 mL CF_3CH_2OH solution of $[Mn^{II}(N4py)(OTf)](OTf)$ (21.6 mg, 0.012 mmol). The resulting mixture was stirred on the bench at 25 °C for 15 min. The cloudy green solution of $[Mn^{IV}(O)(N4py)]^{2+}$ (15 mM) was then filtered through a 0.45 μm membrane to remove unreacted PhIO. Because $[Mn^{IV}(O)(N4py)]^{2+}$ reacts with ethanol at room temperature, the solution was cooled to −40 °C in a freezer and diluted to 7.5 mM with 2.0 mL cold ethanol (−40 °C). The sample was then transferred to a precooled MCD cell at −80 °C, and flash frozen in liquid N_2. MCD spectra were collected on a Jasco circular dichroism spectrometer (J-815) interfaced with an Oxford Instruments magneto-cryostat (SM-4000-8) capable of a horizontal field up to 8 T and a temperature range of 2−300 K. VTVH MCD data were analyzed using a fitting program developed by Neese.[67]

Electronic Structure Computations. All calculations were performed using the program package ORCA 3.0.3.[68] The molecular coordinates for $[Mn^{IV}(O)(N4py)]^{2+}$ were obtained by DFT geometry optimization, as described previously.[54] Structures of $[Mn^{IV}(O)(N4py)]^{2+}$ with nonequilibrium bond lengths, used to evaluate the effect of the Mn^{IV}-oxo bond perturbations on ligand-field state energies, were generated through a relaxed surface scan. In these calculations, the Mn^{IV}-oxo distance was systematically varied from 1.50 to 1.95 Å and fixed during geometry optimization while all other structural parameters were energy-minimized. Cartesian coordinates for all optimized structure are included in the Supporting Information (Tables S1and S2). Electronic transition energies were determined by the time-dependent (TD) DFT method[69−73] using the B3LYP functional,[74−76] with TZVP basis sets on Mn, O, and N, and SVP basis sets on C and H.[77,78] The RIJCOSX approximation, along with TZV/J and SV/J auxiliary basis sets, were employed. TD-DFT-computed absorption spectra were generated by modeling each transition with a Gaussian band with a full width at-half-maximum of 2500 cm^{-1}, and assuming that the calculated oscillator strength (f) is related to the extinction coefficient (ε_{max}) and full-width at half-maximum ($\nu_{1/2}$) as follows: $f = (4.61 \times 10^{-9})(\varepsilon_{max}\nu_{1/2})$. Molecular orbitals were visualized using gOpenMol.[79,80]

The electronic structure of $[Mn^{IV}(O)(N4py)]^{2+}$ was further investigating using CASSCF/NEVPT2 calculations. The results of these calculations were highly sensitive to both the active space employed and the basis set size. Use of a modest active space of CAS(3,5), including only the Mn^{IV} 3d orbitals and electrons, led to a doublet ground state, even after NEVPT2 correction. This is incompatible with EPR studies of $[Mn^{IV}(O)(N4py)]^{2+}$, which reveal a quartet ground state.[41] The quartet-doublet splitting gradually increased with increasing active space. The best agreement between theory and experiment was obtained using CAS(11,9), where the active space consisted of the five Mn^{IV} 3d orbitals (three electrons), the two oxo p_π MOs and one oxo p_σ MO (six electrons), and the Mn^{IV}−N4py σ-bonding MO (two electrons). Optimal results were also obtained using the large def2-TZVPP basis set on Mn, N, and O, with def2-TZVP on C and H. Presumably a larger active space, and larger basis functions, would lead to more accurate results, but such computations were not feasible due to convergence issues. CASSCF/NEVPT2 calculations used for the electronic transitions energies of $[Mn^{IV}(O)(N4py)]^{2+}$ (equilibrium geometry) involved calculating 10 quartet and 40 doublet roots (i.e., including all ligand-field-derived states). Calculations for points along the Mn^{IV}-oxo surface scan considered 6 quartet, 4 doublet, and 1 sextet roots. All CASSCF calculations were tightly converged and employed a 0.8 eV level shifting, which was necessary to achieve convergence. Initial guess orbitals for the CASSCF calculation were quasi-restricted orbitals (QROs) obtained from DFT computations, or taken from a CASSCF wave function from a system of similar geometry. The NEVPT2 method was performed on top of the CASSCF wave function to correct for the lack of dynamic correlation in the CASSCF treatment.[81−83] Similar CASSCF/NEVPT2 calculations were performed for $[Mn^{IV}(O)(OH)(Me_2EBC)]^{+}$ and $[Mn^{IV}(O)(BnTPEN)]^{2+}$ at both the equilibrium geometry (both complexes) and structures with systematically varied Mn^{IV}-oxo distances ($[Mn^{IV}(O)(BnTPEN)]^{2+}$ only). Structures were obtained through DFT optimizations at the same level of theory employed for $[Mn^{IV}(O)(N4py)]^{2+}$.

RESULTS AND ANALYSIS

Electronic Absorption, MCD, and VTVH MCD Data of $[Mn^{IV}(O)(N4py)]^{2+}$. The electronic absorption spectrum of $[Mn^{IV}(O)(N4py)]^{2+}$ has been previously described,[41] but detailed band assignments were not made. In this section, we present an analysis of the 298 K electronic absorption spectrum and variable-temperature, 7 T MCD spectra of $[Mn^{IV}(O)(N4py)]^{2+}$ in order to develop spectral assignments. This analysis is further aided by TD-DFT and CASSCF/NEVPT2 computations.

The electronic absorption spectrum of $[Mn^{IV}(O)(N4py)]^{2+}$ is characterized by a prominent near-infrared (NIR) feature centered at ∼10 500 cm^{-1}, a slow rise in absorption intensity from ∼14 000 to 24 000 cm^{-1}, and the onset of high-intensity features above 25 000 cm^{-1} (Figure 1, top). Electronic

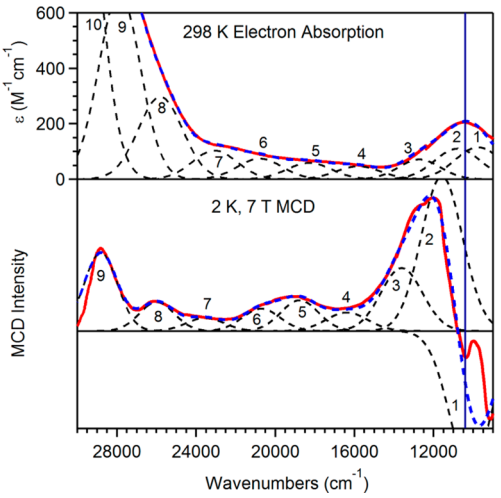

Figure 1. 298 K Electronic absorption spectrum (top) and 2 K, 7 T MCD spectrum of $[Mn^{IV}(O)(N4py)]^{2+}$ in CF_3CH_2OH and 1:1 CF_3CH_2OH:CH_3CH_2OH, respectively. Individual Gaussian curves (dashed black traces) and their sums (dashed blue traces) obtained from iterative fits of the absorption and MCD data are displayed on their respective spectra. The vertical line at 10 500 cm^{-1} shows the close correspondence between the near-IR absorption maxima and the center of the MCD pseudo-A term. Due to instrument limitations, the MCD data were unable to be collected below 9500 cm^{-1}. The notches in the MCD spectra at ∼10 000 and ∼12 500 cm^{-1} are artifacts of the instrument detector and have been observed in other samples.[85]

absorption spectra collected to 5000 cm^{-1} reveal no additional features (Figure S1). The low-temperature MCD spectrum reveals considerably more information regarding the near-IR and visible bands of $[Mn^{IV}(O)(N4py)]^{2+}$ (Figure 1, bottom). All MCD features from 9000 to 30 000 cm^{-1} show an increased intensity at lower temperatures (C-term behavior; see Figure S2),[84] and are attributed to electronic transitions originating from the $^4B_1$ ground state of $[Mn^{IV}(O)(N4py)]^{2+}$. (In our

DOI: 10.1021/jacs.6b08661
J. Am. Chem. Soc. 2016, 138, 15413−15424

discussion of electronic structure, we will assume the coordinate system in Scheme 1 and C_{4v} symmetry, which is a reasonable, approximate symmetry when considering the Mn^{IV} center and the coordinating atoms.) The most prominent feature in the MCD spectrum of $[Mn^{IV}(O)(N4py)]^{2+}$ is a pseudo-*A* term (derivative-shaped *C*-term) centered at 10 800 cm^{-1}, the negative component of which is not fully resolved due to instrument limitations. The center of the pseudo-*A* term is in close correspondence with the maxima of the near-IR absorption band (Figure 1, vertical blue line), suggesting that the electronic transitions contributing to this absorption band give rise to the pseudo-*A* term. Pseudo-*A* terms arise from excited states with perpendicular transition moments (M_i and M_j) that spin−orbit mix along an orthogonal axis (L_k). The MCD spectrum of $[Mn^{IV}(O)(N4py)]^{2+}$ also has less intense, positive features near 19 000, 26 000, and 29 000 cm^{-1} (Figure 1, bottom).

A Gaussian deconvolution of the electronic absorption and MCD spectra of $[Mn^{IV}(O)(N4py)]^{2+}$ reveals a minimum of 10 transitions from 9000 to 30 000 cm^{-1} (Figure 1 and Table S3). The relatively high oscillator strengths for bands 8−10, as well as their low MCD intensities (Table S3), permit their assignment as ligand-to-metal charge-transfer (LMCT) transitions. These transitions could arise from oxo-to-manganese(IV) excitations or excitation from the pyridine π-system of the N4py ligand to the manganese(IV) center. Bands 1 through 7 carry considerably less absorption intensity and are attributed to Mn^{IV} d-d transitions or weak LMCT bands. VTVH MCD data (Figure S3), where the MCD intensity at a given wavelength is monitored as a function of field at various fixed temperatures, were collected for $[Mn^{IV}(O)(N4py)]^{2+}$ (Figure S3). Our analysis of these data, which is limited given that zero-field splitting parameters have not been determined for $[Mn^{IV}(O)(N4py)]^{2+}$, is presented in the Supporting Information.

Electronic Structure of $[Mn^{IV}(O)(N4py)]^{2+}$. The DFT-derived ligand-field splitting pattern for $[Mn^{IV}(O)(N4py)]^{2+}$ shown in Figure 2 is the classic pattern for a metal-oxo species in a tetragonal environment. The t_{2g}-derived orbitals are split into nonbonding $b_2(d_{xy})$ and Mn^{IV}-oxo π-antibonding $e(d_{xz}, d_{yz})$ MOs.[86] Each of these MOs is singly occupied, giving rise to a $b_2(d_{xy})^1$ $e(d_{xz}, d_{yz})^2$ ground configuration and a $^4B_1$ ground state. The unoccupied $b_1(d_{x^2-y^2})$, and $a_1(d_{z^2})$ MOs, which are Mn^{IV}−N4py and Mn^{IV}-oxo σ-antibonding, respectively, lie at higher energy. The compositions and energies of the DFT-computed frontier Kohn−Sham orbitals of $[Mn^{IV}(O)(N4py)]^{2+}$ are collected in Table S7.

Assuming idealized C_{4v} symmetry, four d-d excited states are anticipated for $[Mn^{IV}(O)(N4py)]^{2+}$. The states, configurations, and polarizations describing these transitions are given in Table S8. One-electron excitation from $e(d_{xz}, d_{yz})$ to $b_1(d_{x^2-y^2})$ gives a ^4E excited state; a second ^4E state arises from an $e(d_{xz}, d_{yz}) \rightarrow a_1(d_{z^2})$ one-electron excitation. Because the N4py ligand does not have true 4-fold rotational symmetry, the d_{xz} and d_{yz} orbitals are not actually degenerate (the splitting of the α-spin *e* orbitals is 0.02 eV, or 160 cm^{-1}), so these ^4E states will give rise to two closely spaced electronic transitions. Importantly, a simple group-theory analysis shows that the two components of a given ^4E state will have perpendicular transition moments (M_x and M_y) and spin−orbit couple along L_z. Thus, under ideal conditions, the ^4E (d_{xz}, $d_{yz} \rightarrow d_{x^2-y^2}$) and ^4E (d_{xz}, $d_{yz} \rightarrow d_{z^2}$) excited states should each give an MCD pseudo-*A* term. One of these excited states must be responsible

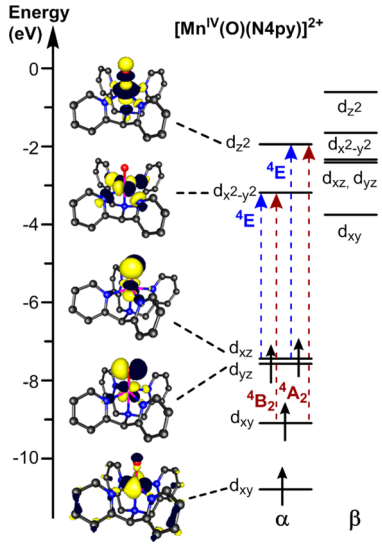

Figure 2. DFT-calculated Mn^{IV} d orbital splitting pattern for $[Mn^{IV}(O)(N4py)]^{2+}$. The spin-allowed d-d transitions, which arise from one-electron orbital excitations (see Table S8), are indicated with dashed arrows. Surface contour plots of α-spin Mn^{IV}-based orbitals are provided adjacent to the orbital diagrams.

for the pseudo-*A* term centered at 10 500 cm^{-1} (Figure 1). The two remaining $b_2(d_{xy}) \rightarrow b_1(d_{x^2-y^2})$ and $b_2(d_{xy}) \rightarrow a_1(d_{z^2})$ excitations of the Mn^{IV} center give $^4B_2$ and $^4A_2$ excited states, respectively (Table S8). Each of these transitions is electric-dipole forbidden in the idealized C_{4v} symmetry but will become allowed through low-symmetry mixing.

TD-DFT and CASSCF/NEVPT2 Computations for $[Mn^{IV}(O)(N4py)]^{2+}$. Assignments for the electronic transitions of $[Mn^{IV}(O)(N4py)]^{2+}$ were facilitated using TD-DFT and CASSCF/NEVPT2 computations. The TD-DFT-computed absorption spectrum of $[Mn^{IV}(O)(N4py)]^{2+}$ bears a strong resemblance to the experimental spectrum, consisting of a low-energy feature at 12 700 cm^{-1} (band *i*), a weak band at ∼21 000 cm^{-1} (band *ii*), and more intense features above 25 000 cm^{-1} (band *iii*; see Figure 3, bottom). Band *i* corresponds to the experimental near-IR absorption at 10 500 cm^{-1}, which is composed of bands 1 and 2 and gives the MCD pseudo-*A* term (Figure 1). The TD-DFT computations overestimate the energy of this band by ∼2000 cm^{-1}, which is well within the accuracy of this method.[87] Band *i* arises from the ^4E (d_{xz}, $d_{yz} \rightarrow d_{x^2-y^2}$) excited state (Table 1). Because the d_{xz} and d_{yz} orbitals are nondegenerate, the components of the ^4E state are split in energy by 60 cm^{-1} in the TD-DFT calculations (Table S9). Importantly, these excited states should appear as an MCD pseudo-*A* term, as discussed in the previous section. On this basis, bands 1 and 2 are attributed to the components of the ^4E (d_{xz}, $d_{yz} \rightarrow d_{x^2-y^2}$) excited state (Table 1).

Band *ii* in the TD-DFT spectrum of $[Mn^{IV}(O)(N4py)]^{2+}$ has contributions from two weak oxo-to-manganese(IV) LMCT transitions at 19 150 and 19 452 cm^{-1} and the components of the ^4E (d_{xz}, $d_{yz} \rightarrow d_{z^2}$) excited state at 20 924 and 20 933 cm^{-1}. On the basis of these results, bands 3 and 4, which are fairly weak in both the absorption and MCD spectra of $[Mn^{IV}(O)(N4py)]^{2+}$, are assigned as LMCT transitions.[88] Bands 5 and 6, which carry greater MCD intensity, are attributed to the components of the ^4E (d_{xz}, $d_{yz} \rightarrow d_{z^2}$) excited state (Table 1). The low oscillator strengths of the LMCT transitions (bands 3 and 4) can be understood by considering the relevant donor

DOI: 10.1021/jacs.6b08661
J. Am. Chem. Soc. 2016, 138, 15413−15424

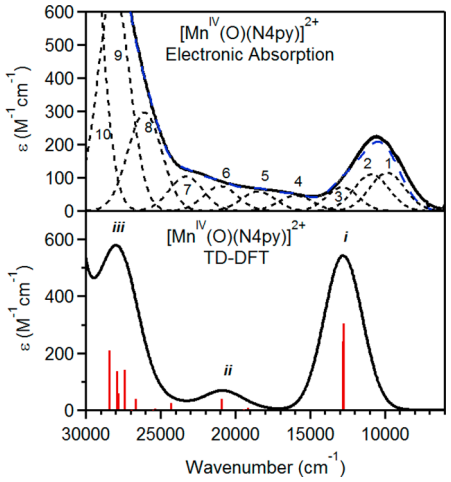

Figure 3. Top: Experimental electronic absorption spectrum of $[Mn^{IV}(O)(N4py)]^{2+}$ with individual Gaussian curves (dashed black traces) and their sums (dashed blue trace) obtained from iterative fits of the absorption and MCD data. Bottom: TD-DFT-calculated electronic absorption spectrum of $[Mn^{IV}(O)(N4py)]^{2+}$. Red sticks represent individual electronic transitions.

and acceptor orbitals. The donor orbitals are the oxo p_π MOs (p_x and p_y), which are the bonding combinations of the Mn^{IV} d_{xz} and d_{yz} MOs plotted in Figure 2. The Mn^{IV} d_{xy} MO is the acceptor orbital. This MO carries very little oxo character, which accounts for the low intensity of band *ii* (Figure 3 and Table S9). Our assignment of bands 5 and 6 to the ^4E (d_{xz}, d_{yz} → d_{z^2}) state is at odds with our expectation that this excited state should give rise to an MCD pseudo-*A* term. However, in the TD-DFT results, these transitions are heavily mixed with the LMCT transitions that occur just at slightly lower energy (Table S9), which could distort the MCD dispersion for these bands. In addition, the close proximity of the ligand-field and LMCT bands could lead to some cancelation of negative and positive signals. We note that Neese and co-workers have invoked similar arguments to explain why a pseudo-*A* term was not observed for the analogous ^3E (d_{xz}, d_{yz} → d_{z^2}) excited state of the $[Fe^{IV}(O)(^{DMM}TPA)(MeCN)]^{2+}$ complex (^{DMM}TPA = tris(3,5-dimethyl-4-methoxypyridyl-2-methyl)amine).[52]

The highest energy TD-DFT band of $[Mn^{IV}(O)(N4py)]^{2+}$ (band *iii*) is dominated by three oxo-to-manganese(IV) LMCT transitions at energies above 27 000 cm^{-1}, but also contains a low-intensity transition to the $^4B_2$ (d_{xy} → $d_{x^2-y^2}$) state at 24 292 cm^{-1} (Figure 3 and Table S9). In this region, the LMCT transitions result from excitation from the oxo p_σ MOs (p_z) to the Mn d_{xy} MO. Bands 8, 9, and 10, which carry significant absorption intensity, are assigned as the LMCT transitions, while band 7, which carries less absorption intensity, is attributed to the $^4B_2$ (d_{xy} → $d_{x^2-y^2}$) state (Table 1).

The TD-DFT-derived band assignments are corroborated by CASSCF/NEVPT2 calculations performed for $[Mn^{IV}(O)(N4py)]^{2+}$ (Table 1). Although more computationally intensive than TD-DFT, the CASSCF/NEVPT2 method is generally considered to be more robust in treating transition-metal excited states,[89,90] and this method has been used previously to treat the excited states of Fe^{IV}-oxo complexes.[33,52] The CASSCF/NEVPT2 calculations for $[Mn^{IV}(O)(N4py)]^{2+}$ predict a pair of low-energy transitions at 7176 and 7552 cm^{-1}, which arise from the ^4E (d_{xz}, d_{yz} → $d_{x^2-y^2}$) excited state. Although the energies of these states are lower than those of bands 1 and 2, the calculated transition energies consistently shifted to higher energy with increased active space and basis set size. Thus, it is possible that better agreement with experiment could be achieved by further increasing these parameters. Components of the ^4E (d_{xz}, d_{yz} → d_{z^2}) state are predicted at 17 085 and 17 252 cm^{-1}, which, is in very good agreement with the experimental energies of bands 5 and 6 and TD-DFT results (Table 1). A pair of LMCT transitions are also predicted in this region (20 620 and 20 873 cm^{-1}), consistent with experiment (Table 1). Overall, the CASSCF/NEVPT2 results nicely corroborate the spectral assignments, although the ligand-field transitions energies tend to be underestimated.

MCD Pseudo-*A* Term Analysis for $[Mn^{IV}(O)(N4py)]^{2+}$. In cases where excited states are reasonably described by one-electron orbital excitations relative to the ground-state configuration, the sign of the MCD *C*-term can be predicted by determining transition moment and spin−orbit vectors through a graphical analysis of the relevant MOs.[67] This approach has been utilized by Solomon,[91] Tuczek,[92] and Brunold[93] to determine signs of MCD pseudo-*A* terms from charge-transfer transitions. Neese has recently determined MCD signs for the d-d transitions of the Fe^{IV}-oxo complex $[Fe^{IV}(O)(^{DMM}TPA)(NCMe)]^{2+}$ using this method.[52] This analysis is used here to demonstrate that the MCD pseudo-*A* term of $[Mn^{IV}(O)(N4py)]^{2+}$ at 10 500 cm^{-1} (bands 1 and 2) arises from the ^4E (d_{xz}, d_{yz} → $d_{x^2-y^2}$) state rather than ^4E (d_{xz}, d_{yz} → d_{z^2}). This assignment is important, as it has been proposed that hydrogen-atom-transfer reactions of $[Mn^{IV}(O)(N4py)]^{2+}$ involve the ^4E (d_{xz}, d_{yz} → $d_{x^2-y^2}$) excited state.[51]

Table 1. Energies (cm^{-1}) and Assignments of Electronic Transitions for $[Mn^{IV}(O)(N4py)]^{2+}$ from Experimental Data, as Well as TD-DFT and CASSCF/NEVPT2 Computations

band	expt[a]	TD-DFT	NEVPT2	assignment
1, 2	10 250, 11 700	12 758, 12 817	7176, 7552	^4E (d_{xz}, d_{yz} → $d_{x^2-y^2}$)
3	13 750	19 150	20 620	LMCT (oxo p_π → Mn^{IV} d_{xy})
4	16 550	19 452	20 873	LMCT (oxo p_π → Mn^{IV} d_{xy})
5, 6	18 955, 20 915	20 924, 20 933	17 085, 17 252	^4E (d_{xz}, d_{yz} → d_{z^2})
7	23 770	24 292	23 076	$^4B_2$ (d_{xy} → $d_{x^2-y^2}$)
8	26 240	27 392[b]	26 236[c]	LMCT (oxo → Mn^{IV})
9	29 100	27 898[b]	ND[d]	LMCT (oxo → Mn^{IV})

[a]Experimental band energies obtained from deconvolution of the MCD spectrum of $[Mn^{IV}(O)(N4py)]^{2+}$. [b]The TD-DFT calculations predict these LMCT transitions to involve donation from the oxo p_z MO to the Mn^{IV} d_{xy} MO. [c]The CASSCF/NEVPT2 calculations predict this LMCT transition to involve donation from the oxo p_y MO to the Mn^{IV} d_{yz} MO. [d]Only 10 quartet states were considered in the CASSCF/NEVPT2 computations. The 10th state is a two-electron ligand-field excited state, which would not be expected to give rise to an electronic absorption band as intense as band 9.

DOI: 10.1021/jacs.6b08661
J. Am. Chem. Soc. 2016, 138, 15413−15424

We first determined the MCD sign of the lower-energy component, ^4E_x ($d_{xz} \rightarrow d_{x^2-y^2}$), where d_{xz} is the donor MO, d_{yz} is the mixing MO, and $d_{x^2-y^2}$ is the acceptor MO. Surface contour plots of the relevant MOs are shown in Figure 4. We

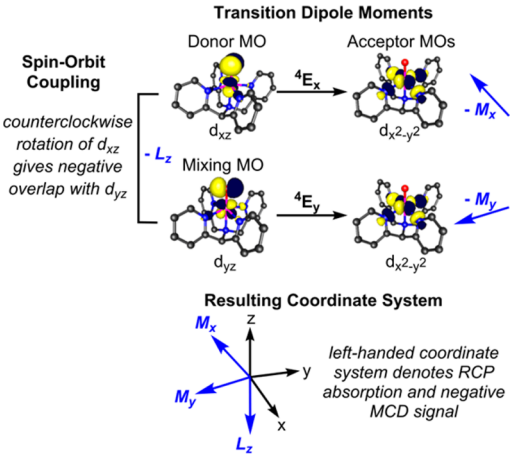

Figure 4. Graphical analysis of pseudo-*A* term sign for ^4E (d_{xz}, $d_{yz} \rightarrow d_{x^2-y^2}$) excited state. The signs and directions of transition dipole moments (M_x and M_y) were determined from the "overlap" of donor (d_{xz}), mixing (d_{yz}), and acceptor ($d_{x^2-y^2}$) MOs. The sign of the spin–orbit coupling vector (L_z) was determined through the rotation properties of the donor and mixing MOs. The resulting left-handed coordinate system of the transition dipole moment and spin–orbit coupling vectors requires absorption of a right-circularly polarized (RCP) photon.

first evaluated the transition dipole moments, M_i, of the individual ^4E_x ($d_{xz} \rightarrow d_{x^2-y^2}$) and ^4E_y ($d_{yz} \rightarrow d_{x^2-y^2}$) components. The transition moments are determined by the sum of the ligand N 2p orbitals following the one-electron excitation (the pure Mn^{IV} *d* orbitals are orthogonal and need not be considered[52]). For ^4E_x ($d_{xz} \rightarrow d_{x^2-y^2}$), the N 2p "overlap" between the donor (d_{xz}) and acceptor ($d_{x^2-y^2}$) orbitals leads to loss of N 2p density along the $+x$ axis and gain of density along the $-x$ axis, resulting in a transition dipole moment along the $-x$ direction ($-M_x$). The corresponding analysis for the ^4E_y ($d_{yz} \rightarrow d_{z^2-y^2}$) transition dipole results in a $-M_y$ vector. The spin–orbit vector is determined by the "overlap" of the higher-energy d_{xz} MO with the d_{yz} MO following a counterclockwise rotation (or a clockwise rotation of the lower-energy MO into the higher-energy MO). This procedure leads to destructive overlap, resulting in $-L_z$. Together, the transition dipole moments and the spin–orbit vector create a left-handed coordinate system (Figure 4), which requires absorption of right-circularly polarized (RCP) light. This would give a negative MCD signal for the ^4E_x ($d_{xz} \rightarrow d_{x^2-y^2}$) state. A corresponding analysis for the ^4E_y ($d_{yz} \rightarrow d_{x^2-y^2}$) component flips the sign of the L_z vector, resulting in prediction of a positive MCD feature.

From this analysis, the expected pseudo-*A* term for ^4E (d_{xz}, $d_{yz} \rightarrow d_{x^2-y^2}$) should consist of a lower-energy negative feature and a higher-energy positive feature, as observed for bands 1 and 2 of $[Mn^{IV}(O)(N4py)]^{2+}$ (Figure 1). A corresponding analysis for the ^4E (d_{xz}, $d_{yz} \rightarrow d_{z^2}$) state, which is presented in Figure S5, predicts a pseudo-*A* term where the lower-energy feature is positively signed, and the higher-energy feature is negatively signed. This is opposite to that observed for bands 1 and 2. Thus, the graphical analysis supports assignment of the MCD pseudo-*A* term at 10 500 cm^{-1} to the ^4E (d_{xz}, $d_{yz} \rightarrow d_{x^2-y^2}$) state, consistent with the TD-DFT and CASSCF computations. We note that our MCD analysis is consistent with a corresponding analysis of the ^3E (d_{xz}, $d_{yz} \rightarrow d_{x^2-y^2}$) and ^3E (d_{xz}, $d_{yz} \rightarrow d_{z^2}$) states of $[Fe^{IV}(O)(^{DMM}TPA)(NCMe)]^{2+}$.[52]

Electronic Structure of $[Mn^{IV}(O)(N4py)]^{2+}$ along the Mn^{IV}-Oxo Reaction Coordinate. Our MCD studies of $[Mn^{IV}(O)(N4py)]^{2+}$ have identified several low-energy excited states, some of which relate to previous DFT computations exploring hydrogen-atom and oxygen-atom-transfer reactivity of Mn^{IV}-oxo species.[39,51] In this section, we use CASSCF/NEVPT2 calculations to understand how these excited states evolve as a function of Mn-oxo elongation, i.e., along the reaction coordinate in the absence of external substrate. This approach has been previously applied to understand the influence of excited-state potential energy surfaces on the reactivity of both synthetic and biological Fe^{IV}-oxo species.[12,33,94] Although this analysis does not include the impact of the Mn^{IV}-oxo–substrate interaction on the Mn^{IV}-oxo states, it provides a conceptual framework for linking excited-state

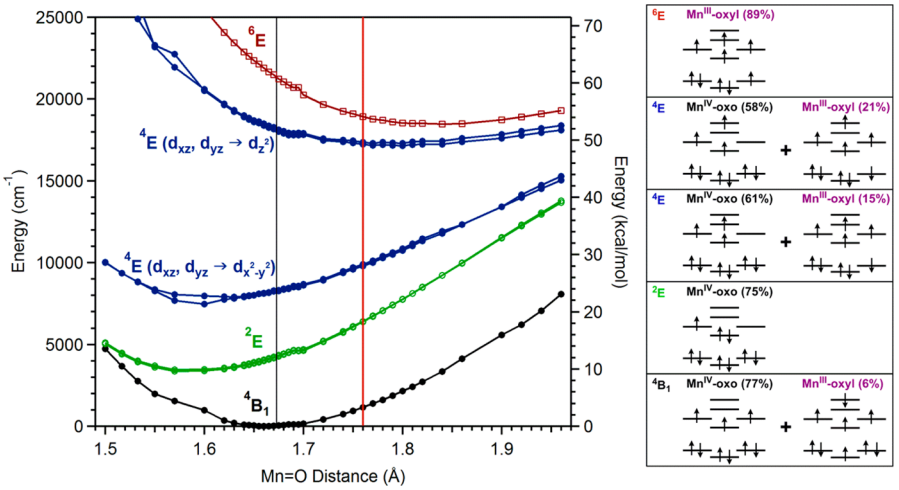

Figure 5. Potential energy surfaces of the lowest-energy states of $[Mn^{IV}(O)(N4py)]^{2+}$ as a function of the Mn=O distance. Energies were obtained from CASSCF/NEVPT2 calculations. The leading configurations for each state are shown in the right-hand panels, with percentages pertaining to the equilibrium Mn=O distances.

DOI: 10.1021/jacs.6b08661
J. Am. Chem. Soc. 2016, 138, 15413–15424

spectroscopic data with electronic structure contributions to reactivity. Moreover, the excited-state reactivity of Mn^{IV}-oxo centers has been predicted to be operative in both hydrogen-atom-transfer[51] and oxygen-atom-transfer reactions.[39] This would tend to imply that the excited-state reactivity is a manifestation of intrinsic properties of the Mn^{IV}-oxo species and does not depend solely on interactions with a particular substrate.

Potential energy surfaces for the ground and several excited states of $[Mn^{IV}(O)(N4py)]^{2+}$, computed at the CASSCF/NEVPT2 level, are shown in Figure 5. The black vertical line in Figure 5 represents the equilibrium Mn-oxo distance of 1.673 Å, and the red vertical line marks the hydrogen-atom-transfer transition-state distance from previous DFT computations (1.76 Å). In the CASSCF approach, each state is described according to leading electronic configurations. The occupancy for the frontier MOs for the relevant configurations are shown in the right-hand panels of Figure 5, and surface contour plots of the frontier MOs are included in Figure 6. The CASSCF MOs are quite similar to the DFT-derived MOs shown in Figure 2 but are less covalent.

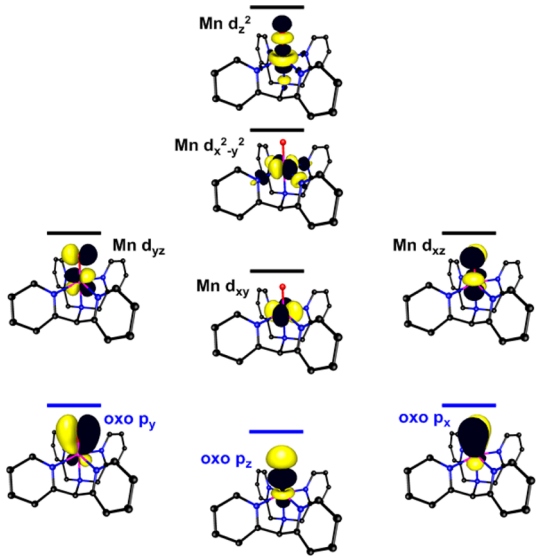

Figure 6. Surface contour plots of frontier MOs from CASSCF calculations for $[Mn^{IV}(O)(N4py)]^{2+}$ at the equilibrium geometry.

At the equilibrium Mn^{IV}-oxo distance, the $^4B_1$ ground state is dominated by the (oxo p_z)^2(oxo p_x, p_y)^4(Mn d_{xy})^1(Mn d_{xz}, d_{yz})^2 configuration, with only 6% contribution from a Mn^{III}-oxyl configuration (S = 1 Mn^{III} coupled to an S = 1/2 oxyl radical). The Mn^{III}-oxyl configuration is related to the ground configuration by an oxo p_z to Mn^{IV} d_{z^2} one-electron excitation and will be referred to as Mn^{III}-oxyl(σ). This configuration creates a hole in a low-lying oxo orbital oriented along the Mn=O vector (the oxo p_z MO; see Figure 6), which, in principle, could facilitate hydrogen-atom transfer by the so-called σ-pathway. The energy of the $^4B_1$ state increases steadily as the Mn-oxo distance is elongated (Figure 5), but the composition of the $^4B_1$ wave function remains fairly static. This is demonstrated in Figure 7 (top), which shows the percent contributions of the leading configurations as a function of Mn=O distance. At the transition-state distance of 1.76 Å, the Mn^{III}-oxyl(σ) character has only increased to 8% of the overall wave function. Insofar as oxyl character is important for

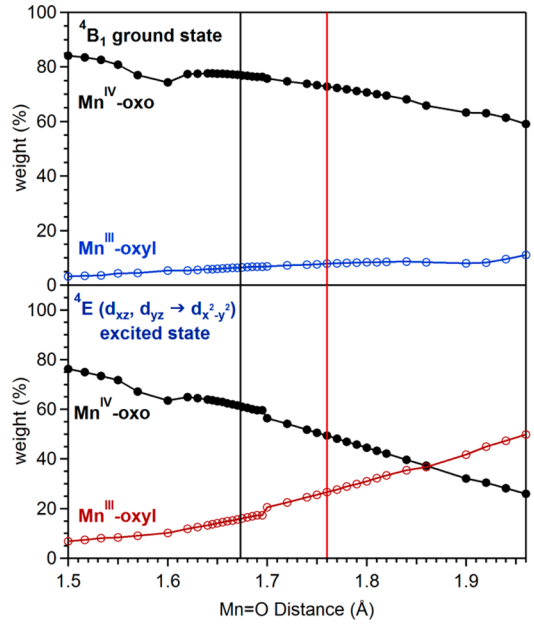

Figure 7. Percent contributions from leading electronic configurations of the $^4B_1$ ground state (top) and $^4E(d_{xz}, d_{yz} \rightarrow d_{x^2-y^2})$ excited state (bottom) as a function of Mn=O distance for $[Mn^{IV}(O)(N4py)]^{2+}$. Vertical lines mark the Mn=O distances at the equilibrium (black) and transition-state (red) geometries.

mediating hydrogen-atom transfer, the low oxyl character in the ground state is in accordance with the high transition-state energy for the $^4B_1$ surface from previous DFT calculations.[39,51] Moreover, the behavior of the Mn^{IV}-oxo ground state is quite different than that observed in CASSCF/CASPT2 calculations for the S = 2 Fe^{IV}-oxo complex $[Fe^{IV}(O)(TMG_3tren)]^{2+}$ (TMG_3tren =1,1,1-tris(2-(N2-(1,1,3,3-tetramethylguanidino))-ethyl)amine).[33] In that case the ground-state wave function carried ~45% Fe^{III}-oxyl(σ) character near the transition state, and this was proposed to facilitate hydrogen-atom transfer by the σ-pathway involving the Fe^{IV} d_{z^2} and oxo p_z orbitals.

The lowest-lying excited states from the CASSCF/NEVPT2 calculations on $[Mn^{IV}(O)(N4py)]^{2+}$ are a nearly degenerate pair of doublet states, which arise from an (oxo p_z)^2(oxo p_y, p_x)^4(Mn d_{xy})^2(Mn d_{xz}, d_{yz})^1 configuration (^2E in Figure 5). These states are only 4300 cm^{-1} above the $^4B_1$ ground state at the equilibrium geometry, and they increase in energy as the Mn-oxo bond is elongated. At very short Mn-oxo distances, when the splitting between the Mn d_{xy} and (d_{xz}, d_{yz}) MOs is large due to stronger Mn-oxo π-interactions, these doublet states become nearly degenerate with the $^4B_1$ ground state (Figure 5). Given their close energetic proximity to the ground state, the ^2E state could, in principle, offer an alternative reaction channel for hydrogen-atom transfer. Indeed, DFT calculations for the reaction of $[Mn^{IV}(O)(N4py)]^{2+}$ with cyclohexadiene predicted a fairly low-energy transition state on the doublet surface of 16.2 kcal/mol (5700 cm^{-1}).[39] Our CASSCF/NEVPT2 calculations suggest that this transition state involves the ^2E state identified here, which is ~5000 cm^{-1} above the $^4B_1$ ground state (Figure 5). However, utilization of the doublet surface for hydrogen-atom transfer requires an initial spin crossing from the $^4B_1$ ground state, and subsequent spin crossing is necessary to reach the stable sextet spin state of the Mn^{III} center of the intermediate generated following hydrogen-atom transfer (Scheme 1). These spin crossings will

DOI: 10.1021/jacs.6b08661
J. Am. Chem. Soc. 2016, 138, 15413−15424

introduce additional barriers for reactivity, as noted previously.[39] Thus, these ^{2}E states, although low in energy, are likely not conduits for hydrogen-atom transfer.

Slightly above the ^{2}E state lies the ^{4}E (d_{xz}, d_{yz} → $d_{x^2-y^2}$) excited state (Figure 5). The components of the ^{4}E (d_{xz}, d_{yz} → $d_{x^2-y^2}$) state are observed experimentally near 10 000 cm^{-1} (bands 1 and 2, Table 1). As previously noted, the CASSCF/NEVPT energies are in good agreement with their experimental counterparts (~8300 cm^{-1}).[95] From the CASSCF/NEVPT2 calculations, the ^{4}E (d_{xz}, d_{yz} → $d_{x^2-y^2}$) energy relative to the ^{4}B$_1$ surface increases slightly to ~9900 cm^{-1} at the transition-state distance of 1.76 Å (Figure 5). The destabilization of ^{4}E (d_{xz}, d_{yz} → $d_{x^2-y^2}$) during Mn=O elongation is attributed to a decrease in energy of the Mn^{IV} d_{xz} and d_{yz} MOs caused by weakened Mn-oxo π-interactions. At the equilibrium Mn=O distance of 1.67 Å, the ^{4}E (d_{xz}, d_{yz} → $d_{x^2-y^2}$) wave function carries a 15% contribution from the (oxo p_z)^2(oxo p_y, p_x)^3(Mn d_{xy})^1(Mn d_{xz}, d_{yz})^2(Mn $d_{x^2-y^2}$)^1 configuration (Figure 5, right). This configuration creates a hole in the oxo $p_{x,y}$ orbitals and will be described as Mn^{III}-oxyl(π). At the transition state, the weight of the Mn^{III}-oxyl(π) configuration has increased to ~25% of the ^{4}E (d_{xz}, d_{yz} → $d_{x^2-y^2}$) wave function, and Mn^{III}-oxyl(π) is the dominant configuration beyond 1.85 Å (Figure 7, bottom). Thus, although the ^{4}E (d_{xz}, d_{yz} → $d_{x^2-y^2}$) state is higher in energy than the ground state, the greater oxyl character could, potentially, better facilitate hydrogen-atom transfer. The nature of the oxyl character, Mn^{III}-oxyl(π), would also suggest a π-pathway for hydrogen-atom transfer, which requires substrate approach perpendicular to the Mn=O vector. Together, these results support previous DFT computations, which found that the ^{4}E (d_{xz}, d_{yz} → $d_{x^2-y^2}$) excited state, with high Mn^{III}-oxyl character and a transition-state geometry suggestive of a π-type hydrogen-atom transfer, led to a lower-energy transition state than the ^{4}B$_1$ ground state.[51]

The central difference between the CASSCF/NEVPT2 and DFT results is the energy of the ^{4}E (d_{xz}, d_{yz} → $d_{x^2-y^2}$) excited state, which is much lower in the DFT calculations that include substrate. This has been observed in previous calculations for Fe^{IV}-oxo complexes.[33] Specifically, CASSCF/CASPT2 calculations for [Fe^{IV}(O)(TMG$_3$tren)]$^{2+}$ predict ligand-field and charge-transfer excited states ~4000 and 8000 cm^{-1} (11 and 23 kcal/mol), respectively, above the electronic ground state at the transition-state Fe=O distance of ~1.76 Å. In contrast, the DFT-calculated transitions-state energies for σ-attack, utilizing the ground state, and π-attack, utilizing the excited states, is only 3 kcal/mol. In that study, the greater stabilization of the excited states upon interaction with substrate was attributed to those excited states being better prepared for hydrogen-atom transfer.[33] We propose that the ^{4}E (d_{xz}, d_{yz} → $d_{x^2-y^2}$) excited state of [Mn^{IV}(O)(N4py)]$^{2+}$ is also well-prepared for hydrogen-atom transfer, leading to its stabilization relative to ^{4}B$_1$ in the presence of substrate. We expand upon this proposal in the Discussion.

In contrast to the ^{4}E (d_{xz}, d_{yz} → $d_{x^2-y^2}$) excited state, whose energy relative to the ^{4}B$_1$ ground state remains fairly constant with Mn=O elongation, the ^{4}E (d_{xz}, d_{yz} → d_{z^2}) and ^{6}E states are stabilized relative to ^{4}B$_1$ at longer Mn=O distances (Figure 5). The potential energy surfaces for these states show energy minima around 1.76 and 1.80 Å, respectively. The ^{4}E (d_{xz}, d_{yz} → d_{z^2}) state has significant Mn^{III}-oxyl character at all Mn=O distances, but increases from 21% at the equilibrium distance to 36% at the transition-state distance. The ^{6}E state arises from a high-spin Mn^{III} center ferromagnetically coupled to an S = 1/2 oxyl radical. Although the large Mn^{III}-oxyl character of these states could suggest they should be quite reactive for hydrogen-atom transfer, the energies of these states are very high. Even at a Mn=O distance of 1.80 Å, the ^{4}E (d_{xz}, d_{yz} → $d_{x^2-y^2}$) and ^{6}E states lie ~17 000−18 000 cm^{-1} (~50 kcal/mol) above the ^{4}B$_1$ ground state. These results are in agreement with our spectroscopic data, which predict a high energy for the ^{4}E (d_{xz}, d_{yz} → $d_{x^2-y^2}$) state (see Table 1), and with previous DFT calculations that predict a high transition-state barrier for hydrogen-atom transfer on the sextet surface.[51]

DISCUSSION

Manganese(IV)-oxo complexes have been implicated in a variety of synthetic and biologically important hydrogen- and oxygen-atom-transfer reactions. Although many mononuclear Mn^{IV}-oxo species are rather sluggish oxidants, only reacting with fairly activated C−H bonds at modest rates,[15,62,64,96,97] several recently reported Mn^{IV}-oxo adducts are capable of attacking more obdurate substrates with reaction rates approaching those of Fe^{IV}-oxo analogues.[38,39,41] Detailed computational studies of the more reactive Mn^{IV}-oxo species have suggested a complicated reaction landscape, where both hydrogen- and oxygen-atom-transfer reactions are facilitated by electronic excited states offering fairly low transition-state barriers (Scheme 1). In this study we have provided detailed insight into the excited-state electronic properties of [Mn^{IV}(O)(N4py)]$^{2+}$, which is one of the more reactive Mn^{IV}-oxo species.[34,35,37] Our spectroscopic data were used as a basis for developing potential energy surfaces along the hydrogen-atom-transfer reaction coordinate in the absence of an external substrate (Figure 5). These data also provide experimental corroboration for a previously predicted excited-state reactivity model based on DFT computations for [Mn^{IV}(O)(N4py)]$^{2+}$.[39,51] Collectively, the results of our combined experimental and theoretical investigations can be used to compare Mn^{IV}-oxo complexes with disparate reactivity and evaluate DFT-based predictions regarding the excited-state reactivity of [Mn^{IV}(O)(N4py)]$^{2+}$.

Comparison of Mononuclear Mn^{IV}-Oxo Complexes: [Mn^{IV}(O)(N4py)]$^{2+}$, [Mn^{IV}(O)(BnTPEN)]$^{2+}$, and [Mn^{IV}(O)(OH)(Me$_2$EBC)]$^{+}$. The handful of nonporphyrinic, mononuclear Mn^{IV}-oxo complexes known to mediate hydrogen-atom-transfer reactions show reaction rates spanning 4 orders of magnitude.[38,41,60,62,97,98] The [Mn^{IV}(O)(BnTPEN)]$^{2+}$,[38] [Mn^{IV}(O)(N4py)]$^{2+}$,[40,41] and [Mn(O)(OH)(Me$_2$EBC)]$^{+}$[65] complexes shown in Figure 8 serve as representative examples.

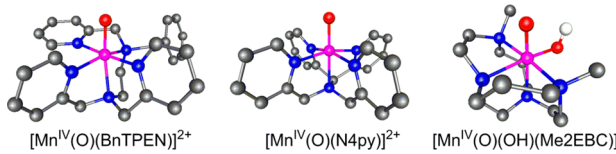

Figure 8. Molecular structures of [Mn^{IV}(O)(BnTPEN)]$^{2+}$, (left) [Mn^{IV}(O)(N4py)]$^{2+}$ (center), and [Mn^{IV}(O)(OH)(Me$_2$EBC)]$^{+}$ (right).

These complexes all feature Mn^{IV}-oxo units in a tetragonal geometry and show C−H bond oxidation rates decreasing in the order [Mn^{IV}(O)(BnTPEN)]$^{2+}$ > [Mn^{IV}(O)(N4py)]$^{2+}$ > [Mn^{IV}(O)(OH)(Me$_2$EBC)]$^{+}$.[99] In the Supporting Information, we discuss bonding comparisons between these complexes that are useful for evaluating frontier MO theory as a tool for

DOI: 10.1021/jacs.6b08661
J. Am. Chem. Soc. 2016, 138, 15413−15424

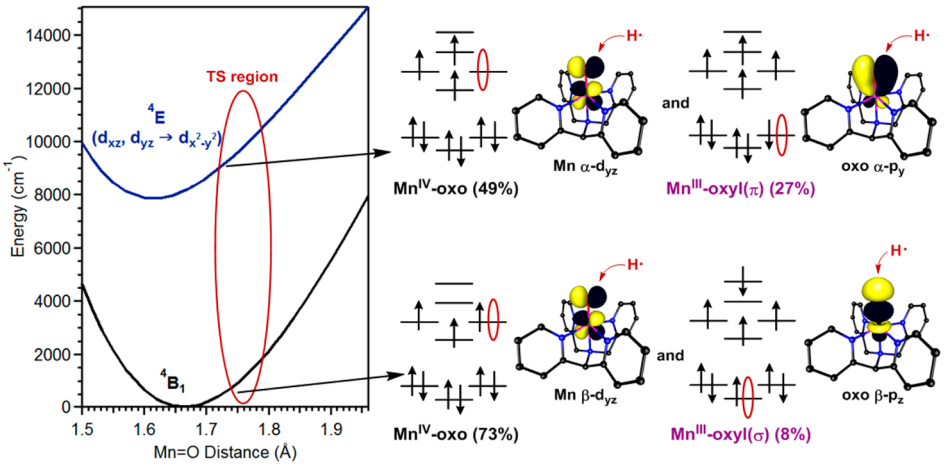

Figure 9. Representation of CASSCF/NEVPT2 potential energy surfaces for $^4B_1$ ground state and ^4E (d_{xz}, d_{yz} → $d_{x^2-y^2}$) excited state (left) and dominant configurations contributing to the CASSCF wave functions (right). The red ellipses in the configuration diagrams represent electron-accepting orbitals for hydrogen-atom transfer involving these configurations. Surface contour plots of these orbitals are shown next to their corresponding configuration diagrams.

understanding their reactivity. Our comparisons of [Mn^{IV}(O)(N4py)]$^{2+}$ and [Mn^{IV}(O)(OH)(Me$_2$EBC)]$^+$ are facilitated by detailed spectral assignments for both complexes.[61] This analysis suggests that the Mn^{IV}-oxo bonding in [Mn^{IV}(O)(N4py)]$^{2+}$, [Mn^{IV}(O)(BnTPEN)]$^{2+}$, and [Mn^{IV}(O)(OH)(Me$_2$EBC)]$^+$ is quite similar, with the perturbations in electronic transition energies largely reflective of differences of the supporting ligands. Consequently, it is challenging to understand the variations in hydrogen-atom-transfer reactivity on the basis of oxo character in the orbitals of the electronic ground state (Table S9).

However, there is a correlation between the energy of the near-IR absorption maxima of these complexes and their hydrogen-atom-transfer reaction rates. The near-IR absorption maxima increase in the order [Mn^{IV}(O)(BnTPEN)]$^{2+}$ (9600 cm^{-1}),[38] < [Mn^{IV}(O)(N4py)]$^{2+}$ (10 500 cm^{-1}), < [Mn^{IV}(O)(OH)(Me$_2$EBC)]$^+$ (11 500 cm^{-1}).[61] Thus, for this very limited set of complexes, a lower-energy absorption band correlates with a faster rate of hydrogen-atom transfer. This relationship could imply the involvement of this excited state in the hydrogen-atom-transfer process.

Accordingly, we investigated the excited-state properties of [Mn^{IV}(O)(BnTPEN)]$^{2+}$ and [Mn^{IV}(O)(OH)(Me$_2$EBC)]$^+$ using CASSCF/NEVPT2 calculations. Unfortunately, even with a large CAS(11,15) active space, we were unable to achieve reasonable agreement with the experimental excited-state energies for [Mn^{IV}(O)(OH)(Me$_2$EBC)]$^+$ (differences between experiment and theory were greater than 5000 cm^{-1}). However, CASSCF/NEVPT2 calculations for [Mn^{IV}(O)(BnTPEN)]$^{2+}$ at its equilibrium geometry predict the components of the ^{4}E (d_{xz}, d_{yz} → $d_{x^2-y^2}$) excited state at 6200 cm^{-1} (Figure S7), in acceptable agreement with the experimental near-IR absorption maximum near 9600 cm^{-1}. Importantly, these calculations, predict a modest red-shift of this excited state relative to that of [Mn^{IV}(O)(N4py)]$^{2+}$, in reasonable agreement with the experimental shift of ∼1000 cm^{-1}. The energy splitting between the $^4B_1$ and ^{4}E (d_{xz}, d_{yz} → $d_{x^2-y^2}$) states of [Mn^{IV}(O)(BnTPEN)]$^{2+}$ is insensitive to the Mn=oxo distance (Figure S7). At the transition-state Mn=O separation of 1.76 Å, the ^{4}E (d_{xz}, d_{yz} → $d_{x^2-y^2}$) excited state is still 6200 cm^{-1} above the $^4B_1$ ground state. The ^{4}E (d_{xz}, d_{yz} → $d_{x^2-y^2}$) state of [Mn^{IV}(O)(BnTPEN)]$^{2+}$ also has slightly greater Mn^{III}-oxyl(π) character compared to [Mn^{IV}(O)(N4py)]$^{2+}$ (30 and 25% oxyl character at the transition-state distance, respectively; cf. Figures 8 and S9). In comparison the $^4B_1$ ground state of [Mn^{IV}(O)(BnTPEN)]$^{2+}$ has very minor oxyl character of 10% at the transition-state Mn=O distance. Thus, while the ground-state bonding descriptions of [Mn^{IV}(O)(BnTPEN)]$^{2+}$ and [Mn^{IV}(O)(N4py)]$^{2+}$, are quite similar the ^{4}E (d_{xz}, d_{yz} → $d_{x^2-y^2}$) excited state of [Mn^{IV}(O)(BnTPEN)]$^{2+}$ has both a lower energy and a greater oxyl character compared with that of [Mn^{IV}(O)(N4py)]$^{2+}$. These factors could account for the enhanced hydrogen-atom-transfer rate observed for [Mn^{IV}(O)(BnTPEN)]$^{2+}$.[38]

The present analysis provides support for the excited-state reactivity model, but it is not without caveats. This comparison is complicated by the difference in charge and ligand-type for the [Mn^{IV}(O)(OH)(Me$_2$EBC)]$^+$ complex, as well as the different solvent used for the reactivity studies.[65] These changes relative to [Mn^{IV}(O)(N4py)]$^{2+}$ and [Mn^{IV}(O)(BnTPEN)]$^{2+}$ could very well contribute to the observed differences in hydrogen-atom-transfer reaction rates. In addition, it is unknown if the near-IR absorption maxima correlate with some other parameter, such as Mn^{IV} reduction potential, that could also explain trends in the reaction rates. What is currently lacking is a set of Mn^{IV}-oxo complexes where systematic changes in ligand electronic properties can be correlated with reactivity data collected under common experimental conditions.

Excited-State Reactivity of [Mn^{IV}(O)(N4py)]$^{2+}$: Oxyl Character and Thermodynamic Driving Force. The excited-state reactivity proposed by Nam and Shaik offers an intriguing model for understanding hydrogen-atom transfer for [Mn^{IV}(O)(N4py)]$^{2+}$ and related Mn^{IV}-oxo complexes.[39,51] Our spectroscopic data provide unambiguous experimental support that the near-IR electronic absorption band of [Mn^{IV}(O)(N4py)]$^{2+}$ is due to the low-lying ^{4}E (d_{xz}, d_{yz} → $d_{x^2-y^2}$) excited state proposed to participate in hydrogen-atom transfer. Our CASSCF/NEVPT2 calculations for [Mn^{IV}(O)(N4py)]$^{2+}$ also predict that the ^{4}E (d_{xz}, d_{yz} → $d_{x^2-y^2}$) excited state has substantially more Mn^{III}-oxyl character than the $^4B_1$ ground state (Figure 7). Manganese-oxo bond elongation, such as that expected along the hydrogen-atom-transfer reaction coordinate, increases the Mn^{III}-oxyl character in the excited state. These

DOI: 10.1021/jacs.6b08661
J. Am. Chem. Soc. 2016, 138, 15413−15424

results, which are also in excellent agreement with previous DFT investigations,[39,51] could explain why the ^{4}E (d_{xz}, d_{yz} → $d_{x^2-y^2}$) state has a lower barrier for hydrogen-atom transfer. Greater oxyl character is commonly assumed to lead to enhanced reactivity.[100,101] However, there is an alternative explanation for the lower-energy transition state on the ^{4}E surface.

Saouma and Mayer have postulated that transition-state energies for different spin surfaces largely reflect the driving force on those particular surfaces (i.e., application of the Bell-Evans-Polayni principle).[32] This is born out in the DFT calculations exploring hydrogen-atom transfer by $[Mn^{IV}(O)(N4py)]^{2+}$. In calculations with cyclohexane as substrate, hydrogen-atom transfer on the ground-state ^{4}B$_1$ surface is uphill by 20.2 kcal/mol, while the process on the excited-state ^{4}E (d_{xz}, d_{yz} → $d_{x^2-y^2}$) surface is uphill by only 10.0 kcal/mol.[51] Thus, the difference in transition-state energy could reflect the difference in driving force rather than the oxyl character.

Importantly, this difference in driving force can be understood on the basis of the leading electronic configurations contributing to the CASSCF/NEVPT2 wave functions for the ^{4}B$_1$ and ^{4}E (d_{xz}, d_{yz} → $d_{x^2-y^2}$) states. The ^{4}B$_1$ state consists predominantly of a (oxo p_z)^2(oxo p_y, p_x)^4(Mn d_{xy})^1(Mn d_{xz}, d_{yz})^2 configuration (Figure 9). Considering only this configuration, the hydrogen-atom-transfer process will involve the transfer of an electron to β-spin d_{xz} or d_{yz} MO. This electron transfer to a partially filled MO incurs a spin-pairing penalty and results in the formation of an unstable intermediate spin (S = 1) Mn^{III} center in the nascent intermediate formed following the hydrogen-atom transfer. This was noted by Nam and Shaik.[51] The formation of an unstable Mn^{III} product will reduce the thermodynamic favorability of this process on the ^{4}B$_1$ surface. The spin pairing energy would be avoided if this process were to utilize the Mn^{III}-oxyl(σ) configuration, which contributes 8% to the ^{4}B$_1$ wave function at the transition-state Mn-oxo distance (Figure 9). This configuration contains a β-spin hole in a low-lying oxo p_z orbital. Transfer of an electron to the oxo p_z MO would still result in an intermediate-spin (S = 1) Mn^{III} center. While this intermediate avoids spin pairing, it results in an electron in a higher-energy MO (the Mn^{IV} d_{z^2}-based MO; see Figure 9). Consequently, although the oxyl character might suggest inherent reactivity, the generation of a higher-energy Mn^{III} intermediate will dampen the reactivity. Consequently, electron-transfer processes on the ^{4}B$_1$ surface result in the formation of a Mn^{III} intermediate with an excited configuration, explaining the unfavorable thermodynamic driving force for this pathway.

Alternatively, the configurations describing the ^{4}E (d_{xz}, d_{yz} → $d_{x^2-y^2}$) excited-state CASSCF/NEVPT2 wave function are better prepared for hydrogen-atom transfer, insofar as they lead to a Mn^{III} intermediate with a low-energy electronic configuration. In fact, they lead to the $(d_{xy})^1(d_{xz}, d_{yz})^2(d_{x^2-y^2})^1$ configuration, which is expected to be the ground-state configuration of the Mn^{III}-hydroxo intermediate following hydrogen-atom transfer. This is true whether one considers either the Mn^{IV}-oxo or Mn^{III}-oxyl(π) configurations that dominate the ^{4}E (d_{xz}, d_{yz} → $d_{x^2-y^2}$) wave function at the transition state (Figure 9). The Mn^{IV}-oxo configuration contributing to ^{4}E (d_{xz}, d_{yz} → $d_{x^2-y^2}$) contains a hole in an α-spin d_{xz} or d_{yz} orbital; thus, transfer of an electron to one of these orbitals results in the formation of high-spin Mn^{III} intermediate with a $(d_{xy})^1(d_{xz}, d_{yz})^2(d_{x^2-y^2})^1$ configuration, and any spin-paring penalty is avoided. Along the same lines, the Mn^{III}-oxyl(π) configuration would result in electron-transfer to a low-lying oxyl π-type orbital, also generating a high-spin Mn^{III} intermediate (Figure 9). Thus, while the transition-state energies reflect the overall thermodynamic driving force on a given spin surface, the basis for the thermodynamic energies can be understood using orbital arguments. This is useful, as it is often quite difficult to establish accurate driving forces for hydrogen-atom-transfer reactions from experiment, especially for the more reactive metal-oxo adducts.

Finally, it could be argued that greater Mn^{III}-oxyl character in the ^{4}E (d_{xz}, d_{yz} → $d_{x^2-y^2}$) wave function would better facilitate hydrogen-atom-transfer processes by these oxidants. This would certainly follow frontier MO theory arguments, which would predict the hole in the lower-energy oxo orbital would result in a more electrophilic oxidant than a hole in a Mn-based d_{xz} or d_{yz} MO. However, the most powerful predictors of reactivity are those which can be subjected to straightforward experimental interrogation. It is difficult to predict how to make chemical changes to Mn^{IV}-oxo complexes to increase Mn^{III}-oxyl character in this excited state. Lower-energy oxo-to-Mn^{IV} LMCT bands could facilitate Mn^{III}-oxyl character through configuration interaction, but it is not obvious how to stabilize these LMCT excited states. Alternatively, the excited-state reactivity model makes the more general prediction that a lower-energy ^{4}E (d_{xz}, d_{yz} → $d_{x^2-y^2}$) excited state should also facilitate more rapid hydrogen-atom-transfer processes, regardless of whether the Mn^{IV}-oxo or Mn^{III}-oxyl(π) configuration dominates. This prediction could be tested experimentally through judicious choice of ligand derivatives. A weakening of the Mn^{IV} equatorial ligand field should provide a stabilization of the $d_{x^2-y^2}$ acceptor orbital, lowering the ^{4}E (d_{xz}, d_{yz} → $d_{x^2-y^2}$) excited state. If this excited state is utilized for hydrogen-atom-transfer reactivity, this should then increase the corresponding reaction rate.

CONCLUSIONS

In this study, we have investigated the ground- and excited-state properties of $[Mn^{IV}(O)(N4py)]^{2+}$, which is one of the more reactive Mn^{IV}-oxo complexes, using a combination of electronic absorption, MCD, and VTVH MCD spectroscopies and DFT and CASSCF/NEVPT2 computations. A graphical analysis was used to predict the sign of MCD C-terms, which led to the unambiguous assignment of bands 1 and 2 to the ^{4}E (d_{xz}, d_{yz} → $d_{x^2-y^2}$) excited state. This is the same excited state implicated in hydrogen- and oxygen-atom-transfer reactions by previously reported DFT computations.[39,51] Thus, our data provide experimental support that hydrogen-atom transfer by $[Mn^{IV}(O)(N4py)]^{2+}$ could be mediated by excited-state reactivity. Nonetheless, an important challenge remains in rationalizing the hydrogen-atom-transfer reactivity trends for the diverse set of Mn^{IV}-oxo species reported in the literature. Our comparison of the electronic structures of $[Mn^{IV}(O)(N4py)]^{2+}$ and $[Mn^{IV}(O)(OH)(Me_2EBC)]^{+}$ underscores the influence of the supporting ligand in perturbing spectroscopic properties, when variations in Mn-oxo bonding might actually be quite minor. Detailed kinetic, spectroscopic, and computational studies of additional systems, preferably those with systematically perturbed ligand fields, will be needed to refine further our understanding of the complex Mn^{IV}-oxo reaction landscape.

DOI: 10.1021/jacs.6b08661
J. Am. Chem. Soc. 2016, 138, 15413−15424

■ ASSOCIATED CONTENT

Supporting Information

The Supporting Information is available free of charge on the ACS Publications website at DOI: 10.1021/jacs.6b08661.

Cartesian coordinates for all DFT-optimized models, Gaussian deconvolution of electronic absorption and MCD data of $[Mn^{IV}(O)(Me_2EBC)]^{2+}$, VTVH MCD data analysis, and results of DFT, TD-DFT, and CASSCF/NEVPT2 calculations on the electronic structure and excited-state properties of $[Mn^{IV}(O)(Me_2EBC)]^{2+}$, including Tables S1−S10 and Figures S1−S9 (PDF)

■ AUTHOR INFORMATION

Corresponding Author

*taj@ku.edu

Notes

The authors declare no competing financial interest.

■ ACKNOWLEDGMENTS

This spectroscopic study of $[Mn^{IV}(O)(N4py)]^{2+}$ was supported by the U.S. National Science Foundation (CHE-1056470 to T.A.J.). Data analysis and electronic structure computations continued under support by the U.S. Department of Energy, Office of Science, Office of Basic Energy Sciences, under Award Number DE-SC0016359 (to T.A.J.).

■ REFERENCES

(1) Borovik, A. S. *Chem. Soc. Rev.* **2011**, *40*, 1870−1874.
(2) de Visser, S. P.; Porro, C. S.; Quesne, M. G.; Sainna, M. A.; Munro, A. W. *Curr. Top. Med. Chem.* **2013**, *13*, 2218−2232.
(3) Fukuzumi, S. *Coord. Chem. Rev.* **2013**, *257*, 1564−1575.
(4) Martinez, S.; Hausinger, R. P. *J. Biol. Chem.* **2015**, *290*, 20702−20711.
(5) Mayer, J. M. *Acc. Chem. Res.* **2011**, *44*, 36−46.
(6) McDonald, A. R.; Que, L., Jr. *Coord. Chem. Rev.* **2013**, *257*, 414−428.
(7) Nam, W. *Acc. Chem. Res.* **2015**, *48*, 2415−2423.
(8) Nam, W.; Lee, Y.-M.; Fukuzumi, S. *Acc. Chem. Res.* **2014**, *47*, 1146−1154.
(9) Puri, M.; Que, L., Jr. *Acc. Chem. Res.* **2015**, *48*, 2443−2452.
(10) Ryabov, A. D. *Adv. Inorg. Chem.* **2013**, *65*, 117−163.
(11) Solomon, E. I.; Wong, S. D.; Liu, L. V.; Decker, A.; Chow, M. S. *Curr. Opin. Chem. Biol.* **2009**, *13*, 99−113.
(12) Srnec, M.; Wong, S. D.; Solomon, E. I. *Dalton Trans.* **2014**, *43*, 17567−17577.
(13) Ye, S.; Geng, C.-Y.; Shaik, S.; Neese, F. *Phys. Chem. Chem. Phys.* **2013**, *15*, 8017−8030.
(14) Ye, S.; Neese, F. *Curr. Opin. Chem. Biol.* **2009**, *13*, 89−98.
(15) Yin, G. *Acc. Chem. Res.* **2013**, *46*, 483−492.
(16) Costas, M.; Mehn, M. P.; Jensen, M. P.; Que, L., Jr. *Chem. Rev.* **2004**, *104*, 939−986.
(17) Ray, K.; Pfaff, F. F.; Wang, B.; Nam, W. *J. Am. Chem. Soc.* **2014**, *136*, 13942−13958.
(18) Ray, K.; Heims, F.; Schwalbe, M.; Nam, W. *Curr. Opin. Chem. Biol.* **2015**, *25*, 159−171.
(19) Sahu, S.; Goldberg, D. P. *J. Am. Chem. Soc.* **2016**, *138*, 11410−11428.
(20) Engelmann, X.; Monte-Perez, I.; Ray, K. *Angew. Chem., Int. Ed.* **2016**, *55*, 7632−7649.
(21) Liu, W.; Groves, J. T. *Acc. Chem. Res.* **2015**, *48*, 1727−1735.
(22) Cooper, H. L. R.; Mishra, G.; Huang, X.; Pender-Cudlip, M.; Austin, R. N.; Shanklin, J.; Groves, J. T. *J. Am. Chem. Soc.* **2012**, *134*, 20365−20375.
(23) Planas, O.; Clemancey, M.; Latour, J.-M.; Company, A.; Costas, M. *Chem. Commun. (Cambridge, U. K.)* **2014**, *50*, 10887−10890.
(24) Wong, S. D.; Srnec, M.; Matthews, M. L.; Liu, L. V.; Kwak, Y.; Park, K.; Bell, C. B., III; Alp, E. E.; Zhao, J.; Yoda, Y.; Kitao, S.; Seto, M.; Krebs, C.; Bollinger, J. M.; Solomon, E. I. *Nature (London, U. K.)* **2013**, *499*, 320−323.
(25) Kulik, H. J.; Drennan, C. L. *J. Biol. Chem.* **2013**, *288*, 11233−11241.
(26) Matthews, M. L.; Neumann, C. S.; Miles, L. A.; Grove, T. L.; Booker, S. J.; Krebs, C.; Walsh, C. T.; Bollinger, J. M., Jr. *Proc. Natl. Acad. Sci. U. S. A.* **2009**, *106*, 17723−17728.
(27) Matthews, M. L.; Krest, C. M.; Barr, E. W.; Vaillancourt, F. H.; Walsh, C. T.; Green, M. T.; Krebs, C.; Bollinger, J. M., Jr. *Biochemistry* **2009**, *48*, 4331−4343.
(28) Kulik, H. J.; Blasiak, L. C.; Marzari, N.; Drennan, C. L. *J. Am. Chem. Soc.* **2009**, *131*, 14426−14433.
(29) Vaillancourt, F. H.; Yeh, E.; Vosburg, D. A.; Garneau-Tsodikova, S.; Walsh, C. T. *Chem. Rev. (Washington, DC, U. S.)* **2006**, *106*, 3364−3378.
(30) Galonic, D. P.; Barr, E. W.; Walsh, C. T.; Bollinger, J. M., Jr.; Krebs, C. *Nat. Chem. Biol.* **2007**, *3*, 113−116.
(31) Warren, J. J.; Tronic, T. A.; Mayer, J. M. *Chem. Rev.* **2010**, *110*, 6961−7001.
(32) Saouma, C. T.; Mayer, J. M. *Chem. Sci.* **2014**, *5*, 21−31.
(33) Srnec, M.; Wong, S. D.; England, J.; Que, L.; Solomon, E. I. *Proc. Natl. Acad. Sci. U. S. A.* **2012**, *109*, 14326−14331.
(34) Decker, A.; Rohde, J.-U.; Klinker, E. J.; Wong, S. D.; Que, L., Jr.; Solomon, E. I. *J. Am. Chem. Soc.* **2007**, *129*, 15983−15996.
(35) Decker, A.; Solomon, E. I. *Angew. Chem., Int. Ed.* **2005**, *44*, 2252−2255.
(36) Decker, A.; Rohde, J.-U.; Que, L., Jr.; Solomon, E. I. *J. Am. Chem. Soc.* **2004**, *126*, 5378−5379.
(37) Usharani, D.; Janardanan, D.; Li, C.; Shaik, S. *Acc. Chem. Res.* **2013**, *46*, 471−482.
(38) Wu, X.; Seo, M. S.; Davis, K. M.; Lee, Y.-M.; Chen, J.; Cho, K.-B.; Pushkar, Y. N.; Nam, W. *J. Am. Chem. Soc.* **2011**, *133*, 20088−20091.
(39) Chen, J.; Cho, K.-B.; Lee, Y.-M.; Kwon, Y. H.; Nam, W. *Chem. Commun.* **2015**, *51*, 13094−13097.
(40) Chen, J.; Lee, Y.-M.; Davis, K. M.; Wu, X.; Seo, M. S.; Cho, K.-B.; Yoon, H.; Park, Y. J.; Fukuzumi, S.; Pushkar, Y. N.; Nam, W. *J. Am. Chem. Soc.* **2013**, *135*, 6388−6391.
(41) Leto, D. F.; Ingram, R.; Day, V. W.; Jackson, T. A. *Chem. Commun.* **2013**, *49*, 5378−5380.
(42) Chen, J.; Yoon, H.; Lee, Y.-M.; Seo, M. S.; Sarangi, R.; Fukuzumi, S.; Nam, W. *Chem. Sci.* **2015**, *6*, 3624−3632.
(43) Kim, S.; Cho, K.-B.; Lee, Y.-M.; Chen, J.; Fukuzumi, S.; Nam, W. *J. Am. Chem. Soc.* **2016**, *138*, 10654−10663.
(44) Hage, R.; Lienke, A. *J. Mol. Catal. A: Chem.* **2006**, *251*, 150−158.
(45) Hage, R.; Lienke, A. *Angew. Chem., Int. Ed.* **2006**, *45*, 206−222.
(46) Talsi, E. P.; Bryliakov, K. P. *Coord. Chem. Rev.* **2012**, *256*, 1418−1434.
(47) Lyakin, O.; Ottenbacher, R.; Bryliakov, K.; Talsi, E. *Top. Catal.* **2013**, *56*, 939−949.
(48) Company, A.; Lloret-Fillol, J.; Costas, M. *Small molecule models for nonporphyrinic iron and manganese oxygenases*; Elsevier B.V.: Amsterdam, 2013; pp 487−564.
(49) Gardner, K. A.; Mayer, J. M. *Science* **1995**, *269*, 1849−1851.
(50) Mayer, J. M. *Acc. Chem. Res.* **2011**, *44*, 36−46.
(51) Cho, K.-B.; Shaik, S.; Nam, W. *J. Phys. Chem. Lett.* **2012**, *3*, 2851−2856.
(52) Ye, S.; Xue, G.; Krivokapic, I.; Petrenko, T.; Bill, E.; Que, L., Jr.; Neese, F. *Chem. Sci.* **2015**, *6*, 2909−2921.
(53) Yoon, H.; Lee, Y.-M.; Nam, W.; Fukuzumi, S. *Chem. Commun.* **2014**, *50*, 12944−12946.
(54) Leto, D. F.; Jackson, T. A. *Inorg. Chem.* **2014**, *53*, 6179−6194.

DOI: 10.1021/jacs.6b08661
J. Am. Chem. Soc. 2016, 138, 15413−15424

(55) Ayougou, K.; Bill, E.; Charnock, J. M.; Garner, C. D.; Mandon, D.; Trautwein, A. X.; Weiss, R.; Winkler, H. *Angew. Chem., Int. Ed. Engl.* **1995**, *34*, 343−346.
(56) Kurahashi, T.; Kikuchi, A.; Shiro, Y.; Hada, M.; Fujii, H. *Inorg. Chem.* **2010**, *49*, 6664−6672.
(57) Leto, D. F.; Massie, A. A.; Colmer, H. E.; Jackson, T. A. *Inorg. Chem.* **2016**, *55*, 3272−3282.
(58) Gupta, R.; Taguchi, T.; Lassalle-Kaiser, B.; Bominaar, E. L.; Yano, J.; Hendrich, M. P.; Borovik, A. S. *Proc. Natl. Acad. Sci. U. S. A.* **2015**, *112*, 5319−5324.
(59) Parsell, T. H.; Behan, R. K.; Green, M. T.; Hendrich, M. P.; Borovik, A. S. *J. Am. Chem. Soc.* **2006**, *128*, 8728−8729.
(60) Sawant, S. C.; Wu, X.; Cho, J.; Cho, K.-B.; Kim, S. H.; Seo, M. S.; Lee, Y.-M.; Kubo, M.; Ogura, T.; Shaik, S.; Nam, W. *Angew. Chem., Int. Ed.* **2010**, *49*, 8190−8194.
(61) Chattopadhyay, S.; Geiger, R. A.; Yin, G.; Busch, D. H.; Jackson, T. A. *Inorg. Chem.* **2010**, *49*, 7530−7535.
(62) Yin, G.; Danby, A. M.; Kitko, D.; Carter, J. D.; Scheper, W. M.; Busch, D. H. *J. Am. Chem. Soc.* **2008**, *130*, 16245−16253.
(63) Wang, Y.; Shi, S.; Wang, H.; Zhu, D.; Yin, G. *Chem. Commun.* **2012**, *48*, 7832−7834.
(64) Shi, S.; Wang, Y.; Xu, A.; Wang, H.; Dajian, Z.; Roy, S. B.; Jackson, T. A.; Busch, D. H.; Yin, G. *Angew. Chem., Int. Ed.* **2011**, *50*, 7321−7324.
(65) Yin, G.; Danby, A. M.; Kitko, D.; Carter, J. D.; Scheper, W. M.; Busch, D. H. *J. Am. Chem. Soc.* **2007**, *129*, 1512−1513.
(66) Mallick, D.; Shaik, S. *ACS Catal.* **2016**, *6*, 2877−2888.
(67) Neese, F.; Solomon, E. I. *Inorg. Chem.* **1999**, *38*, 1847−1865.
(68) Neese, F. *Wiley Interdisciplinary Reviews: Computational Molecular Science* **2012**, *2*, 73−78.
(69) Bauernschmitt, R.; Ahlrichs, R. *Chem. Phys. Lett.* **1996**, *256*, 454−464.
(70) Casida, E. M.; Jamorski, C.; Casida, K. C.; Salahub, D. R. *J. Chem. Phys.* **1998**, *108*, 4439−4449.
(71) Hirata, S.; Head-Gordon, M. *Chem. Phys. Lett.* **1999**, *302*, 375−382.
(72) Hirata, S.; Head-Gordon, M. *Chem. Phys. Lett.* **1999**, *314*, 291−299.
(73) Stratmann, R. E.; Scuseria, G. E.; Frisch, M. J. *J. Chem. Phys.* **1998**, *109*, 8218−8224.
(74) Becke, A. D. *J. Chem. Phys.* **1993**, *98*, 1372−1377.
(75) Becke, A. D. *J. Chem. Phys.* **1993**, *98*, 5648−5652.
(76) Lee, C.; Yang, W.; Parr, R. G. *Phys. Rev. B: Condens. Matter Mater. Phys.* **1988**, *37*, 785−789.
(77) Schäfer, A.; Horn, H.; Ahlrichs, R. *J. Chem. Phys.* **1992**, *97*, 2571−2577.
(78) Schäfer, A.; Huber, C.; Ahlrichs, R. *J. Chem. Phys.* **1994**, *100*, 5829−5835.
(79) Laaksonen, L. *J. Mol. Graphics* **1992**, *10*, 33−34.
(80) Bergman, D. L.; Laaksonen, L.; Laaksonen, A. *J. Mol. Graphics Modell.* **1997**, *15*, 301−306.
(81) Angeli, C.; Cimiraglia, R.; Evangelisti, S.; Leininger, T.; Malrieu, J.-P. *J. Chem. Phys.* **2001**, *114*, 10252−10264.
(82) Angeli, C.; Cimiraglia, R.; Malrieu, J.-P. *Chem. Phys. Lett.* **2001**, *350*, 297−305.
(83) Angeli, C.; Cimiraglia, R.; Malrieu, J.-P. *J. Chem. Phys.* **2002**, *117*, 9138−9153.
(84) Piepho, S. B.; Schatz, P. N. *Group Theory in Spectroscopy with Applications to Magnetic Circular Dichroism*; Wiley: New York, 1983; p 634.
(85) Wijeratne, G. B.; Zolnhofer, E. M.; Fortier, S.; Grant, L. N.; Carroll, P. J.; Chen, C.-H.; Meyer, K.; Krzystek, J.; Ozarowski, A.; Jackson, T. A.; Mindiola, D. J.; Telser, J. *Inorg. Chem.* **2015**, *54*, 10380−10397.
(86) Surface contour plots of the α-spin d_{xy} orbitals shown in Figure 2 contain minor ligand contributions. The relatively low energy of these orbitals and the true low symmetry of the complex facilitate some mixing of these MOs.
(87) Neese, F. *JBIC, J. Biol. Inorg. Chem.* **2006**, *11*, 702−711.
(88) The MCD intensity of band 3 is not well defined. In Figure 1 this band carries moderate MCD intensity; however, the MCD intensity of this band decreases dramatically with a modest increase in the width of band 2.
(89) Atanasov, M.; Ganyushin, D.; Sivalingam, K.; Neese, F. *Struct. Bonding (Berlin, Ger.)* **2011**, *143*, 149−220.
(90) Schapiro, I.; Sivalingam, K.; Neese, F. *J. Chem. Theory Comput.* **2013**, *9*, 3567−3580.
(91) Yoon, J.; Liboiron, B. D.; Sarangi, R.; Hodgson, K. O.; Hedman, B.; Solomon, E. I. *Proc. Natl. Acad. Sci. U. S. A.* **2007**, *104*, 13609−13614.
(92) Westphal, A.; Klinkebiel, A.; Berends, H.-M.; Broda, H.; Kurz, P.; Tuczek, F. *Inorg. Chem.* **2013**, *52*, 2372−2387.
(93) Craft, J. L.; Mandimutsira, B. S.; Fujita, K.; Riordan, C. G.; Brunold, T. C. *Inorg. Chem.* **2003**, *42*, 859−867.
(94) Srnec, M.; Wong, S. D.; Matthews, M. L.; Krebs, C.; Bollinger, J. M.; Solomon, E. I. *J. Am. Chem. Soc.* **2016**, *138*, 5110−5122.
(95) This energy is slightly different than the values listed in Table 1, as a smaller number of roots were used in the surface-scan calculations.
(96) Barman, P.; Vardhaman, A. K.; Martin, B.; Wörner, S. J.; Sastri, C. V.; Comba, P. *Angew. Chem., Int. Ed.* **2015**, *54*, 2095−2099.
(97) Garcia-Bosch, I.; Company, A.; Cady, C. W.; Styring, S.; Browne, W. R.; Ribas, X.; Costas, M. *Angew. Chem., Int. Ed.* **2011**, *50*, 5648−5653.
(98) Parsell, T. H.; Yang, M.-Y.; Borovik, A. S. *J. Am. Chem. Soc.* **2009**, *131*, 2762−2763.
(99) Unfortunately, kinetic comparisons using a common substrate have not been published for these complexes. However, rate data using ethylbenzene establish $[Mn^{IV}(O)(BnTPEN)]^{2+}$ as 5-fold more reactive than $[Mn^{IV}(O)(N4py)]^{2+}$, and rate data with dihydroanthracene establish $[Mn^{IV}(O)(N4py)]^{2+}$ as 200-fold more reactive than $[Mn^{IV}(O)(OH)(Me_2EBC)]^{+}$.
(100) Ye, S.; Neese, F. *Proc. Natl. Acad. Sci. U. S. A.* **2011**, *108*, 1228−1233.
(101) Balcells, D.; Raynaud, C.; Crabtree, R. H.; Eisenstein, O. *Inorg. Chem.* **2008**, *47*, 10090−10099.

DOI: 10.1021/jacs.6b08661
J. Am. Chem. Soc. 2016, 138, 15413−15424